Graphical Abstract

A strain energy-based elastic parameter calibration method for lattice/bonded particle modelling of solid materials

Tongming Qu, Y.T. Feng, Jidong Zhao

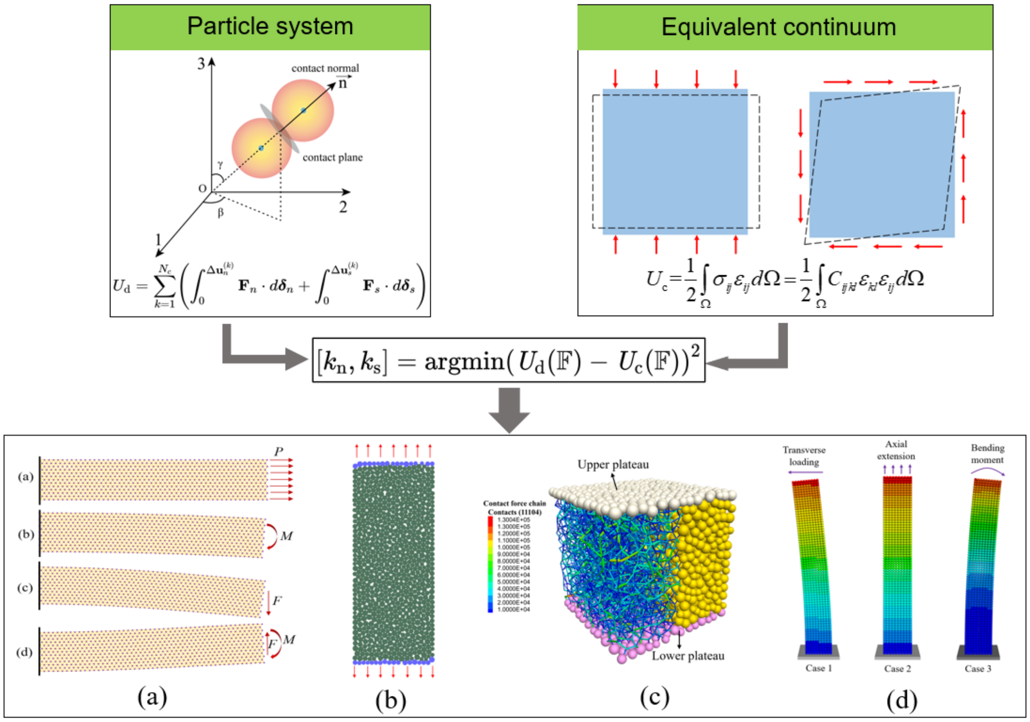

A strain energy-based elastic parameter calibration method for lattice/bonded particle modelling of solid materials

Tongming Qu[a,b], Y.T. Feng[a,*], Jidong Zhao[b,c]

[a] *Zienkiewicz Centre for Computational Engineering College of Engineering Swansea University Swansea Wales SA1 8EP UK*
[b] *Department of Civil and Environmental Engineering Hong Kong University of Science and Technology Clearwater Bay Kowloon Hong Kong SAR China.*
[c] *HKUST Shenzhen-Hong Kong Collaborative Innovation Research Institute Futian Shenzhen China*

Abstract

A generic strain energy-based parameter calibration method is proposed to calibrate the elastic parameters of lattice or bonded-particle modelling of solid materials. Unlike surrogate models or commonly used optimisation-based calibration methods in DEM, this approach does not require running any physical simulations to obtain tentative solutions and thus ensures high calibration efficiency. The novelty of this method is achieved in five aspects: (1) the calibrated parameters are physically decoupled as elastic and strength parameters; (2) the calibration of elastic parameters is converted to an optimisation problem with the goal of minimising the difference of strain energy between the discrete and continuum systems subjected to imposed global strain/deformation fields; (3) the strain energy is analytically determined for circular/spherical particles in both systems; (4) explicit expressions of the gradients of the loss function facilitate obtaining the optimal particle-scale parameters; and (5) when subjected to two independence strain fields, a closed-form solution is derived for a pair of uniform normal and tangential stiffnesses. The proposed calibration framework is validated with four different examples. All the results confirm the reliability of the proposed calibration method in lattice or bonded-particle modelling of solid continua.

---

[*] Corresponding author: y.feng@swansea.ac.uk

Keywords: Parameter calibration, Discrete element method, Lattice bond model, Strain energy, Parallel bond model, Optimisation problem

---

1. Introduction

Solid, as one of the most fundamental states of matter in the universe, is made of atoms or mesoscopic grains which are bound to each other in either a regular lattice (crystalline solids, such as metals) or irregularly packing (amorphous solid, e.g. glass, rocks). The macroscopic deformation and ductile or brittle failure of solid materials thereby originate in grain-scale interactions. For materials which are initially continuous solids but followed by crack and fracture in a physical process, discrete particle-based methods offer the possibility of modelling them in a consistent framework without extra attention [1, 2, 3]. Different particle-based methods can be regarded as different numerical discretisations of physical objects with different degrees of abstractions. Fig. 1 demonstrates three typical discrete particle-based models: (a) bonded block model; (b) bonded particle model and (c) lattice bond model.

The prominent advantages of discrete particle-based methods have motivated numerous applications in the simulation of solid materials, such as concrete [4, 5], rock [6, 7, 8], ceramic [9], and sea ice [10], to name a few. However, calibration of particle-level parameters involved in particle-based methods remains a great challenge which has not been properly resolved [11]. As the parameter calibration is a typical high-dimensional inverse problem, determining optimal parameters is normally conducted in a trial-and-error manner and often requires a large amount of time and effort. Various methods have been developed to accelerate accurate parameter calibration. Generally, existing calibration methods can be roughly classified into three types: (1) analytical models, (2) surrogate models and (3) optimisation methods.

For analytical models, Griffiths and Mustoe [12] adopted a grillage of discrete elements to simulate elastic continua. The use of a regular packing enables the stiffness parameters of discrete elements to be calculated directly. Tavarez and Plesha [13], and Le et al [14] also derived analytical solutions based on a hexagonal 2D elementary volume, where the formulations are the same as the results in Griffiths and Mustoe [12]. Zhao et al. [15] developed a 3D distinct lattice spring model where the relation between micro and macro elastic material properties are established through the hyperelastic theory.

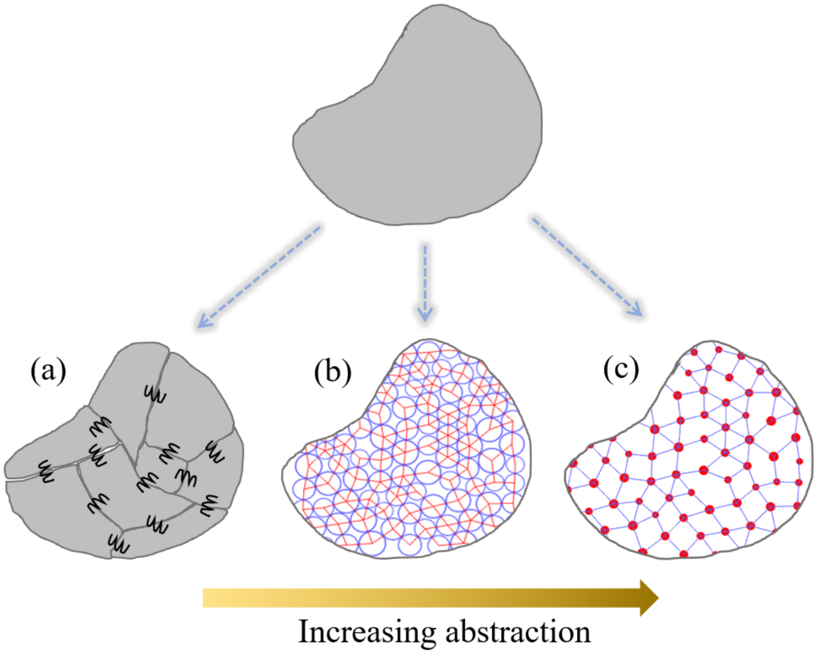

Figure 1: Three types of particle-based modelling of a solid continuum: (a) bonded block model; (b) bonded particle model and (c) lattice bond model.

Jarolin and Dosta [16] proposed a linearisation-based method to calibrate the stiffness parameters of bonded-particle models by solving a linear system of equations. These analytical approaches are efficient in determining the particle-scale parameters but either are limited to a uniform or statistically homogeneous RVE structure, or may not maintain high accuracy for some modelling cases.

Surrogate modelling aims to develop an approximation relation of a real mapping between independent and dependent variables. The reason for using surrogate models for calibration is that the relation between microscopic and macroscopic parameters is too complex to be explicitly characterised. Commonly used surrogate models for calibration include: (1) response surfaces [17, 18], e.g. polynomial and multi-adaptive regression splines (MARS); (2) linear or nonlinear fitting based parametric studies [19, 20, 21]; (3) machine learning methods [22], e.g. artificial neural networks (ANNs) [23, 24], random forests [25] and reinforcement learning [26]; and (4) probabilistic-based surrogate modelling, such as the Bayesian approach [27, 28, 29]. In addition, some experimental design methods, e.g. Taguchi methods [30], Plackett-Burman (PB) and central composite design (CCD) [31, 32], orthogonal experiment design (OED) method [33] and Latin hypercube sampling [34], are also used to sample data strategically and thus reduce the cost of fitting a reliable surrogate model.

Instead of developing a comprehensive surrogate mapping relation, optimisation based methods are goal-oriented with the single aim to discover the optimal microscopic parameters for macroscopic targets. Prevalent optimisation methods that have been employed in parameter calibration include: (1) statistic-based optimisation, such as simulated annealing [35] and Gaussian process regression [36]; (2) population-based optimisation, e.g. Ant-colony optimisation [37], particle swarm optimisation [38, 39], genetic algorithms [40, 41]; (3) surrogate based optimisation [42, 43]; and (4) gradient-based optimisation [44]. Recently, Qu et al. [45] developed a physics-informed gradient-based optimisation framework for the calibration of elastic parameters and cohesive bond strength parameters. The calibration method makes use of existing micromechanics to determine the initial guesses and thus speeds up the optimisation process. However, to calibrate a group of elastic parameters or strength parameters, many physical simulations are still required.

Despite great progress made in this field, most existing algorithms are not always sufficiently generic and efficient. In this study, we develop a generic strain energy-based method for the elastic parameter calibration of two types of particle-based models, i.e. the bonded particle model within the context of the discrete element method (DEM) (Fig. 1b) and the lattice bond model (Fig. 1c). The lattice model can be viewed as a bonded particle-based model with each lattice node as a particle without physical dimensions. Alternatively, any bonded particle-based model for continuum solids can also be conceptually abstracted as a lattice model, where each bonded particle pair is equivalent to one lattice connection except for cases where particle dimensions are explicitly involved in the model. The parameter calibration of these two models can thus be viewed in a unified way and treated equivalently within the current framework.

A unique advantage of this new method is that it does not require running physical simulations to search particle-scale parameters. When a particle packing/lattice is given, a group of reliable particle/lattice level parameters will be automatically obtained. It may be expected that the great improvement in the efficiency of parameter calibration will further promote the application of particle-based methods in unveiling micro-scale deformation and damage mechanisms of solid materials.

The rest of the paper is structured as follows. Section 2 proposes the basic framework of the strain energy-based calibration method and the strategy to obtain the optimal values of the parameters to be calibrated. After a brief revisit of the parallel bond (PB) model, Section 3 demonstrates how to extend the proposed framework to discrete element modelling with the PB model. In Section 4, a series of numerical examples are performed to verify the proposed method. A detailed discussion on the potential origins of calibration errors, extensions to other types of elastic parameter representation methods, and the calibration of non-linear elastic contact models, are given in Section 5. Some concluding remarks are made in Section 6.

It is noted that although both lattice and bonded particle-based models can be used interchangeably in the proposed methodology as previously stated, bonded circular/spherical particle-based models will be primarily used below, for the sake of consistence and clarity in description. Furthermore, unless stated otherwise, the Einstein summation convention is adopted throughout the paper.

2. A strain energy-based parameter calibration method

2.1. The overall framework

A complete particle-based simulation requires both elastic parameters (e.g., Young's modulus and Poisson's ratio) and strength parameters (frictional coefficient, tensile strength and cohesive strength) to characterise reversible elastic deformation and irreversible plastic or brittle instability. For a deformation process incorporating irreversible damages, both types of parameters are intertwined and cannot be differentiated explicitly. The consequence of calibrating all the parameters based on overall observations of a large deformation process is that the parameter space remains unnecessarily large and thus the calibration has to be time-consuming. Also, a greater probability of multiple solutions in a high-dimensional space can affect the calibration quality adversely.

An important but often overlooked fact is that solids can undergo certain elastic deformation without the failure of particle-scale cohesive bonds in a small strain condition. Physical simulations at this stage are simply affected by elastic parameters, without the involvement of strength parameters. We can make use of this fact to decompose the parameter calibration into two separate tasks: one is for the elastic parameters and the other one is for the strength parameters. Such a decoupling strategy will shift a high-dimensional problem to a relatively low-dimensional one and thus effectively simplify the calibration process. Note that the decoupling strategy here is different from the elasticplastic deformation decomposition in the phenomenological constitutive modelling framework. The latter is an assumption under a relatively large deformation condition while the current one is a fact under the small-strain elasticity state. This study will focus on the calibration of elastic parameters for bonded particle models and lattice bond models. The calibration of strength parameters can be referred to our preceding work [45].

The lattice/particle-scale elastic interaction formulation that determines the bond behaviour can be of a linear or non-linear type. Also, even linear elasticity can be characterised in different ways. In the following text, we will introduce a calibration framework with the most widely used combination of normal and tangential stiffnesses (k_n and k_s) in the linear elastic model, under the assumption that a set of uniform k_n and k_s are used to characterise the interaction between two contacting particles or points. The strategy to extend the proposed calibration framework to non-uniform k_n and k_s and other elastic descriptions will be discussed in Section 5.

This calibration method is inspired by the understanding that the strain energy stored in a physical domain and its numerical twin (or counterpart) due to any deformation should be the same or very close to each other if the numerical simulation reproduces the physical entity. The fundamental idea of the parameter calibration is then to search the particle-scale parameters which minimise the difference in strain energy between a bonded particle system and the equivalent continuum subject to a given deformation field $\mathbb{F}$:

$$[k_\mathrm{n}, k_\mathrm{s}] = \mathrm{argmin}\left(U_\mathrm{d}(\mathbb{F}) - U_\mathrm{c}(\mathbb{F}) \right)^2 \tag{1}$$

where U_d and U_c represent the strain energies in both discrete and continuum systems, respectively; argmin returns the optimal k_n and k_s values which minimise the squared difference between U_d and U_c. Different optimal stiffness values may be obtained by imposing different deformation fields though.

2.2. Strain energy in a discrete particle-based system

In this section, the strain energy of a particle-based system will be derived by taking the bonded circular/spherical particle model as an example. The same formulation of the strain energy can be applied equally to a lattice bond model. The strain energy stored between two (bonded) particles is equal to the work done by the interaction forces acting from the undeformed state until the current deformation state specified by a given deformation field $\mathbb{F}$.

For a solid or structure which is idealised or discretised by an assembly of points and their bonds, the entire strain energy of a specimen is the summation of the strain energy stored by all the individual interaction bonds throughout the volume. As the rotation and twisting of two circular/spherical particles do not change the topology of the microstructures of a particle-based assembly, only normal and tangential relative displacements are responsible for changes in strain energy of the equivalent continuum.

Without considering rolling and twisting stiffnesses, the total strain energy stored in the entire discrete system can be given as follows:

$$U_{\mathrm{d}} = \sum_{k=1}^{N_c} \left(\int_0^{\Delta\mathbf{u}_n^{(k)}} \mathbf{F}_n \cdot d\boldsymbol{\delta}_n + \int_0^{\Delta\mathbf{u}_s^{(k)}} \mathbf{F}_s \cdot d\boldsymbol{\delta}_s \right) \tag{2}$$

where $\Delta\mathbf{u}_n^{(k)}$ and $\Delta\mathbf{u}_s^{(k)}$ denote the normal and tangential relative displacements of bond k, respectively; $\mathbf{F}_n$ and $\mathbf{F}_s$ are the interaction forces in the normal and shear directions, respectively; $d\boldsymbol{\delta}_n$ and $d\boldsymbol{\delta}_s$ are infinitesimal deformations in the normal and shear directions, respectively; and N_c is the total number of bonds.

For the linear bond model, the interaction forces can be expressed with relative displacements of particles as follows:

$$\mathbf{F}_n = k_n \Delta\mathbf{u}_n, \mathbf{F}_s = k_s \Delta\mathbf{u}_s \tag{3}$$

where k_n and k_s are the normal and tangential stiffnesses of the bond, respectively; $\mathbf{u}_n$ and $\mathbf{u}_s$ are normal and tangential relative displacements of the bond, respectively. The strain energy stored in bond k with a linear relation is given by:

$$U^{(k)} = \frac{1}{2}(k_n \Delta\mathbf{u}_n^{(k)} \cdot \Delta\mathbf{u}_n^{(k)} + k_s \Delta\mathbf{u}_s^{(k)} \cdot \Delta\mathbf{u}_s^{(k)}) \tag{4}$$

By equating the displacements of particles to the displacements of the corresponding points in the continuum, the relative displacement of particles $\Delta u_i^{(k)}$ can be characterised by the equivalent local strain $\varepsilon_{ij}^{(k)}$ obtained from the given deformation field $\mathbb{F}$ in the continuum as:

$$\Delta u_i^{(k)} = \varepsilon_{ij}^{(k)} L^{(k)} \xi_j^{(k)} \tag{5}$$

where $L^{(k)}$ is the length between the centres of two bonding particles; i and j are indices in $\{1, 2\}$ for 2D, and $\{1, 2, 3\}$ for 3D, with 1, 2, 3 representing

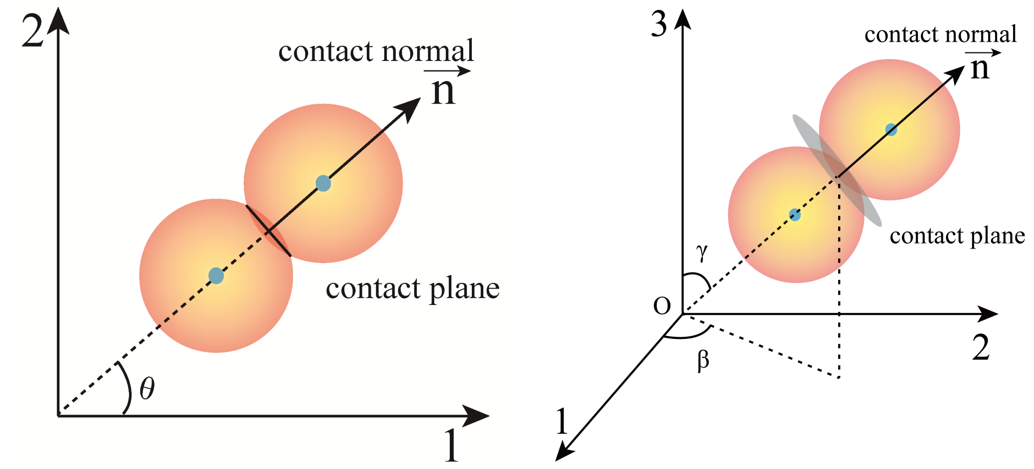

(a) 2D, polar coordinates (b) 3D, spherical coordinates

Figure 2: Two contacting particles in a global coordinate system

x, y, z directions in the global coordinate system. $\xi_j^{(k)}$ is the j^{th} component of the direction vector of bond k. As shown in Fig. 2, in the spherical coordinates (r, θ, φ), $\xi_j^{(k)} = (\xi_1^{(k)}, \xi_2^{(k)}, \xi_3^{(k)}) = (\sin\theta\cos\varphi, \sin\theta\sin\varphi, \cos\theta)$, while in the polar coordinates, $\xi_j^{(k)} = (\xi_1^{(k)}, \xi_2^{(k)}) = (\cos\varphi, \sin\varphi)$. Recalling that the coordinate transformation of displacements, the magnitude (scalar) of normal relative displacement $\Delta u_i^{(k)}$ can be expressed as

$$\Delta u_n^{(k)} = \Delta u_i^{(k)} \xi_i^{(k)} = \varepsilon_{ij}^{(k)} (x_j^{(B)} - x_j^{(A)}) \xi_i^{(k)} = \varepsilon_{ij}^{(k)} L^{(k)} \xi_i^{(k)} \xi_j^{(k)} \tag{6}$$

The normal displacement $\Delta\mathbf{u}_n^{(k)}$ is:

$$\Delta\mathbf{u}_n^{(k)} = \Delta u_n^{(k)} \xi_i^{(k)} \tag{7}$$

The tangential relative displacement $\Delta\mathbf{u}_s^{(k)}$ can be written as

$$\Delta\mathbf{u}_s^{(k)} = \varepsilon_{mn}^{(k)} L^{(k)} \xi_n^{(k)} - \varepsilon_{ij}^{(k)} L^{(k)} \xi_i^{(k)} \xi_j^{(k)} \xi_m^{(k)} \tag{8}$$

Substituting Eqs. (6) and (8) into (4), the energy stored in the particle-based system can be rewritten as:

$$U_{\mathrm{d}} = \sum_{k=1}^{Nc} U^{(k)} = \frac{1}{2} \sum_{k=1}^{N_c} \Bigg[k_n \left(\varepsilon_{ij}^{(k)} L^{(k)} \xi_i^{(k)} \xi_j^{(k)} \right) \left(\varepsilon_{kl}^{(k)} L^{(k)} \xi_k^{(k)} \xi_l^{(k)} \right) + \\ k_s \left(\varepsilon_{mn}^{(k)} L^{(k)} \xi_n^{(k)} - \varepsilon_{ij}^{(k)} L^{(k)} \xi_i^{(k)} \xi_j^{(k)} \xi_m^{(k)} \right) \left(\varepsilon_{nk}^{(k)} L^{(k)} \xi_k^{(k)} - \varepsilon_{lk}^{(k)} L^{(k)} \xi_l^{(k)} \xi_k^{(k)} \xi_m^{(k)} \right) \Bigg] \tag{9}$$

In the case that a compatible strain field ε_{ij} (or equivalent $\mathbb{F}$) is imposed on a specimen, a local strain $\varepsilon_{ij}^{(k)}$ at position $\mathbf{x}$ is required to equal the global strain $\varepsilon_{ij}(\mathbf{x})$ for the corresponding continuum

$$\varepsilon_{ij}^{(k)}(\mathbf{x}) = \varepsilon_{ij}(\mathbf{x}) \tag{10}$$

The strain energy of the discrete system can thus be formulated as:

$$U_{\mathrm{d}} = \frac{1}{2} \sum_{k=1}^{N_{\mathrm{c}}} \left(L^{(k)} \right)^2 \Bigg[k_n \left(\varepsilon_{ij} \xi_i^{(k)} \xi_j^{(k)} \right) \left(\varepsilon_{kl} \xi_k^{(k)} \xi_l^{(k)} \right) + \\ k_s \left(\varepsilon_{mn} \xi_n^{(k)} - \varepsilon_{ij} \xi_i^{(k)} \xi_j^{(k)} \xi_m^{(k)} \right) \left(\varepsilon_{mk} \xi_k^{(k)} - \varepsilon_{lk} \xi_l^{(k)} \xi_k^{(k)} \xi_m^{(k)} \right) \Bigg] \tag{11}$$

2.3. Strain energy in a continuum system

By applying a compatible strain field (can be uniform or position-dependent) to a given domain Ω in a continuum, the stored strain energy U_{c} should be:

$$U_{\mathrm{c}} = \frac{1}{2} \int_{\Omega} \sigma_{ij} \varepsilon_{ij} d\Omega = \frac{1}{2} \int_{\Omega} C_{ijkl} \varepsilon_{kl} \varepsilon_{ij} d\Omega \tag{12}$$

where C_{ijkl} is the elastic stiffness tensor of the material; the expansion of strain energy in the case of a uniform strain field is:

$$U_{\mathrm{c}} = \begin{cases} \frac{1}{2} \left(\sigma_{11} \varepsilon_{11} + \sigma_{12} \gamma_{12} + \sigma_{22} \varepsilon_{22} \right) S & \text{(2D)} \\ \frac{1}{2} \left(\sigma_{11} \varepsilon_{11} + \sigma_{22} \varepsilon_{22} + \sigma_{33} \varepsilon_{33} + \sigma_{12} \gamma_{12} + \sigma_{13} \gamma_{13} + \sigma_{23} \gamma_{23} \right) V & \text{(3D)} \end{cases} \tag{13}$$

where γ_{ij} is the engineering shear strain with $\gamma_{ij} = 2\varepsilon_{ij} (i \neq j)$; S and V represent the area (2D) and volume (3D) of the domain, respectively.

As stated in Section 2.1, a set of reasonable particle-scale parameters should minimise the strain energy between the bonded particle and continuum systems, when subjected to the same imposed strain field. So the calibration of particle-scale parameters can be reformulated into a minimisation problem as:

$$[k_n, k_s] = \operatorname{argmin} \mathbb{L}(k_n, k_s) \tag{14}$$

where the loss function $\mathbb{L}$ can be formulated as:

$$\begin{aligned}\mathbb{L} = \frac{1}{4}\Bigg\{ \int_{\Omega} C_{ijkl}\varepsilon_{kl}\varepsilon_{ij} d\Omega - \sum_{k=1}^{N_c} \left(L^{(k)}\right)^2 \Bigg[k_n \left(\varepsilon_{ij}\xi_i^{(k)}\xi_j^{(k)}\right)\left(\varepsilon_{kl}\xi_k^{(k)}\xi_l^{(k)}\right) + \\ k_s \left(\varepsilon_{mn}\xi_n^{(k)} - \varepsilon_{ij}\xi_i^{(k)}\xi_j^{(k)}{\xi_m}^{(k)}\right)\left(\varepsilon_{mk}\xi_k^{(k)} - \varepsilon_{lk}\xi_l^{(k)}\xi_k^{(k)}\xi_m^{(k)}\right)\Bigg]\Bigg\}^2\end{aligned} \tag{15}$$

2.4. Virtual strain field

To calculate the strain energy of a system, one has to specify the deformation or strain fields applied. Here virtual strain fields are imposed on both the continuum and bonded particle systems and the parameter calibration is performed completely based on virtual strain energies. Fig. 3 demonstrates two virtual loading cases: (1) a compressive strain field, and (2) a pure shear strain field on a 2D domain. These two strain fields are mathematically described as:

$$(1) \begin{bmatrix} 0 & 0 \\ 0 & \delta\varepsilon_{22} \end{bmatrix} \text{(vertical compression)}; \quad (2) \begin{bmatrix} 0 & \delta\varepsilon_{12} \\ \delta\varepsilon_{21} & 0 \end{bmatrix} \text{(pure shear)}$$

where ε_{22} and ε_{12} are infinitesimal compressive or shear components of a virtual strain field, which is equivalent to a virtual linear displacement field in the body. Note that these strain fields applied are completely nominal and no real simulations are performed on the specimens.

For an isotropic solid, the elastic properties of the specimen can be determined provided that two individual elastic parameters are known. Two different strain fields, which can be normal (compressive or tensile) or pure shear strain, are thus required, as will be explained in Section 2.5. Such a selection of loading cases is normally sufficient to calibrate particle-scale parameters for an isotropic solid from a macroscopic perspective.

When considering multiple (N) strain fields, this would be a multi-objective optimisation problem, but can be reduced to a single objective optimisation

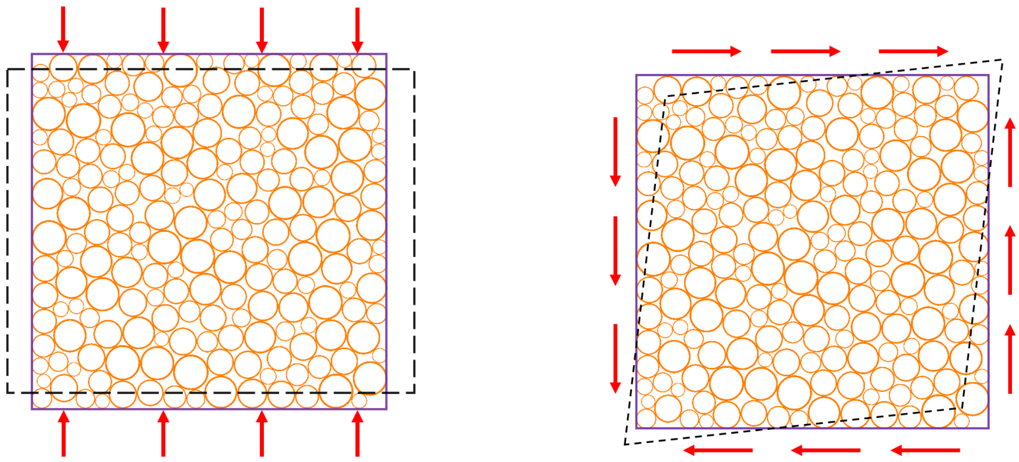

(a) Compressive strain

(b) Shear strain

Figure 3: Schematics of imposed virtual strain fields (2D)

problem with its loss function $\mathbb{L}$ being the average of the corresponding individual loss functions $\mathbb{L}_i$:

$$\mathbb{L} = \frac{1}{N} \sum_{i=1}^{N} \mathbb{L}_i \tag{16}$$

2.5. Simplified calibration solutions for a linear bond model with uniform contact stiffness

For a bonded particle system with a linear bond model and two uniform interaction stiffnesses k_n and k_s, the loss function $\mathbb{L}$ in Eq. (14) is a quadratic function. The first-order gradients of the loss function with respect to k_n and k_s can be derived:

$$\begin{aligned} \frac{\partial \mathbb{L}}{\partial k_n} = -\frac{1}{2} \sum_{k=1}^{N_c} \left(L^{(k)}\right)^2 \left(\varepsilon_{op} \xi_o^{(k)} \xi_p^{(k)}\right) \left(\varepsilon_{qr} \xi_q^{(k)} \xi_r^{(k)}\right) \Bigg\{ \int_\Omega C_{ijkl} \varepsilon_{kl} \varepsilon_{ij} d\Omega - \\ \sum_{k=1}^{N_c} \left(L^{(k)}\right)^2 \Bigg[k_n \left(\varepsilon_{ij} \xi_i^{(k)} \xi_j^{(k)}\right) \left(\varepsilon_{kl} \xi_k^{(k)} \xi_l^{(k)}\right) + \\ k_s \left(\varepsilon_{mn} \xi_n^{(k)} - \varepsilon_{ij} \xi_i^{(k)} \xi_j^{(k)} \xi_m^{(k)}\right) \left(\varepsilon_{mk} \xi_k^{(k)} - \varepsilon_{lk} \xi_l^{(k)} \xi_k^{(k)} \xi_m^{(k)}\right) \Bigg] \Bigg\} \end{aligned} \tag{17}$$

$$
\begin{aligned}
\frac{\partial \mathbb{L}}{\partial k_s} = -\frac{1}{2}\sum_{k=1}^{N_c}\left(L^{(k)}\right)^2 \left(\varepsilon_{op}\xi_p^{(k)} - \varepsilon_{qr}\xi_q^{(\lambda)}\xi_r^{(k)}\xi_o^{(k)}\right)\left(\varepsilon_{st}\xi_t^{(k)} - \varepsilon_{uv}\xi_u^{(k)}\xi_v^{(k)}\xi_s^{(k)}\right) \\
\left\{\int_\Omega C_{jikl}\varepsilon_{kl}\varepsilon_{ij}d\Omega - \sum_{k=1}^{N_c}\left(L^{(k)}\right)^2 \left[k_n\left(\varepsilon_{ij}\xi_i^{(k)}\xi_j^{(k)}\right)\left(\varepsilon_{kl}\xi_k^{(k)}\xi_l^{(k)}\right) + \right.\right. \\
\left.\left. k_s\left(\varepsilon_{mn}\xi_n^{(k)} - \varepsilon_{ij}\xi_i^{(k)}\xi_j^{(k)}\xi_m^{(k)}\right)\left(\varepsilon_{mk}\xi_k^{(k)} - \varepsilon_{lk}\xi_l^{(k)}\xi_k^{(k)}\xi_m^{(k)}\right)\right]\right\} \quad (18)
\end{aligned}
$$

The optimal k_n and k_s that minimise the loss function $\mathbb{L}$ can be found from the conditions

$$
\frac{\partial \mathbb{L}}{\partial k_n} = 0, \quad \frac{\partial \mathbb{L}}{\partial k_s} = 0 \tag{19}
$$

which can be reduced to a linear equation

$$
a_{n1}k_n + b_{s1}k_s = c_1 \tag{20}
$$

where

$$
\begin{aligned}
a_{n1} =& \sum_{k=1}^{N_c}\left(L^{(k)}\right)^2\left(\varepsilon_{ij}\xi_i^{(k)}\xi_j^{(k)}\right)\left(\varepsilon_{kl}\xi_k^{(k)}\xi_l^{(k)}\right) \\
b_{s1} =& \sum_{k=1}^{N_c}\left(L^{(k)}\right)^2\left(\varepsilon_{mn}\xi_n^{(k)} - \varepsilon_{ij}\xi_i^{(k)}\xi_j^{(k)}\xi_m^{(k)}\right)\left(\varepsilon_{mk}\xi_k^{(k)} - \varepsilon_{lk}\xi_l^{(k)}\xi_k^{(k)}\xi_m^{(k)}\right) \\
c_1 =& \int_\Omega C_{jikl}\varepsilon_{kl}\varepsilon_{ij}d\Omega
\end{aligned}
$$

In order to uniquely determine k_n and k_s, one more independent strain field needs to be imposed to the specimen to obtain the second linear equation

$$
a_{n2}k_n + b_{s2}k_s = c_2 \tag{21}
$$

where a_{n2}, b_{s2} and c_2 can be evaluated in a similar way under the second strain field. Then the values of k_n and k_s can be found by solving Eqs. (20) and (21) simultaneously in the following closed form

$$
\begin{cases}
k_n = \dfrac{c_1 b_{s2} - c_2 b_{s1}}{a_{n1}b_{s2} - a_{n2}b_{s1}} \\
k_s = \dfrac{a_{n1}c_2 - a_{n2}c_1}{a_{n1}b_{s2} - a_{n2}b_{s1}}
\end{cases} \tag{22}
$$

Although Eq. (22) can yield a group of unique values for k_n and k_s, different combination of strain fields will give rise to different optimal solutions.

In the case of non-uniform k_n and k_s, i.e., the stiffness values vary from bond to bond, the unique solutions of the unknown stiffnesses (both normal and tangential) can only be obtained provided that the number of unknown stiffnesses is equal to the number of mutually different strain fields imposed. However, it is practically difficult to implement such a large number of strain fields simultaneously. Therefore, the solutions of non-uniform k_n and k_s parameters will have to be sought using other methods. This part of extension will be investigated in our future work.

3. Applications to parallel bond modelling in DEM

The parallel bond (PB) model, originally developed by Potyondy and Cundall [46], is probably the most prevalent model for the simulation of various cohesive solids in the DEM framework [47, 48, 49]. In this section, we attempt to incorporate the parallel bond model into the proposed calibration method. The detailed formulation conversion and simulation requirements are elaborated. Such an extension will enable an efficient calibration for DEM simulations of cohesive interactions between particles using the PB model.

3.1. The formulations of linear parallel bond contacts

The mechanical behaviour of a parallel bond is governed by two separate parts: the first part is equivalent to the linear contact model, while the second part is the parallel bond contact (see Fig. 4). A parallel bond can resist tensile loads and moments when bonded but the linear contact model cannot. These two contact models act in parallel with each other when undergoing external loads. Therefore, for a compressive load, both linear and parallel bond models will act simultaneously. For tensile loads, only the parallel bond part involves computations.

The parallel bond model conceptually implements a group of evenly distributed elastic springs with constant normal and tangential stiffnesses over a cross-section lying on the contact plane. The normal and tangential forces ($\overline{\mathbf{F}}_{\mathrm{n}}$ and $\overline{\mathbf{F}}_{\mathrm{s}}$, respectively) for the parallel bond model are updated as follows:

$$\overline{\mathbf{F}}_{\mathrm{n}} := \overline{\mathbf{F}}_{\mathrm{n}} + \bar{k}_{\mathrm{n}} \bar{A} \Delta \boldsymbol{\delta}_{\mathrm{n}} \tag{23}$$

$$\overline{\mathbf{F}} := \overline{\mathbf{F}}_{\mathrm{s}} - \bar{k}_{\mathrm{s}} \bar{A} \Delta \boldsymbol{\delta}_{\mathrm{s}} \tag{24}$$

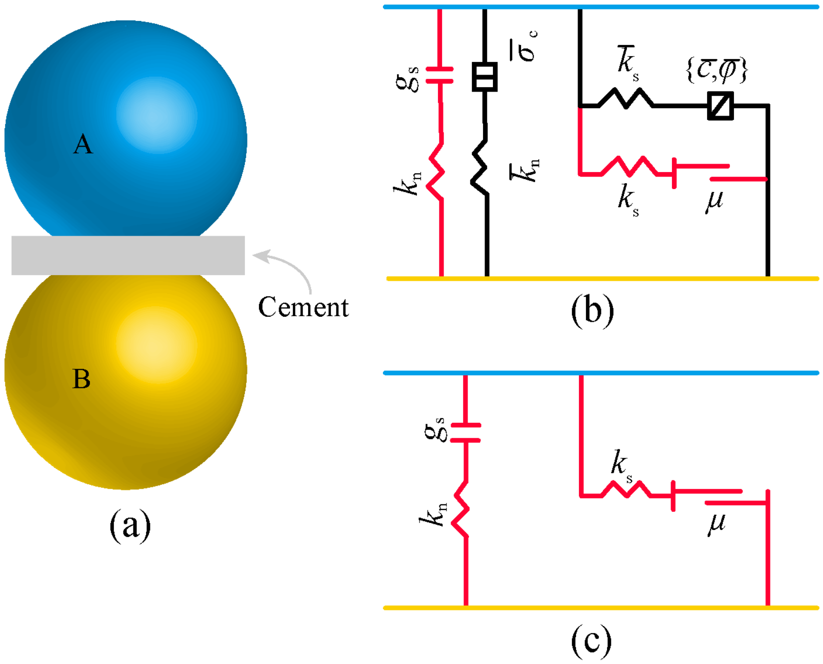

Figure 4: Contact behaviour of a parallel bond contact model: (a) two particles and their contact; (b) bonded contact, and (c) unbonded contact [50]

where $\bar{k}_\text{n}$, $\bar{k}_\text{s}$, $\Delta\boldsymbol{\delta}_\text{n}$ and $\Delta\boldsymbol{\delta}_\text{s}$ are relative normal- and shear- parallel bond stiffnesses and displacement increment, respectively; $\bar{k}_\text{n}$ and $\bar{k}_\text{s}$ represent the unit stiffness over the interaction area, and their dimension is [stress/displacement] while the counterpart for the linear model is [force/displacement]. $\bar{A}$ is the cross-sectional area and its value can be calculated as:

$$\bar{A} = \begin{cases} 2\bar{R}, & \text{2D} \\ \pi\bar{R}^2, & \text{3D} \end{cases}, \text{ with } \bar{R} = \bar{\lambda} \min\left(R^{(1)}, R^{(2)}\right) \tag{25}$$

where $\bar{\lambda}$ is the radius multiplier, and $R^{(1)}$ and $R^{(2)}$ are the radii of the two contacting particles.

3.2. Parameter assignment when using a parallel bond model

The bond stiffness values calibrated from the proposed method are the total stiffnesses of an interaction, similar to the beam stiffness in the beam-particle approach [2]. Considering the basic formulation of a parallel bond model in Section 3.1, a feasible strategy to ensure the same tensile and compressive stiffness when undergoing external loads is by inactivating the linear contact part, i.e. using the parallel bond part only before the damage of contacts occurs. Furthermore, the parallel bond stiffnesses should be converted from the derived stiffnesses as shown below:

$$\bar{k}_n = \frac{k_n}{2\bar{\lambda}\min\left(R^{(1)}, R^{(2)}\right)}, \quad \bar{k}_s = \frac{k_s}{2\bar{\lambda}\min\left(R^{(1)}, R^{(2)}\right)} \tag{26}$$

4. Numerical verifications

Four numerical examples are used to verify the applicability of the proposed strain energy-based calibration methodology to particle-based methods for modelling solid materials. Section 4.1 is a hexagonal cantilever beam subjected to bending moment and end loads; Section 4.2 demonstrates a 2D uniaxial tensile testing case; Section 4.3 gives 3D uniaxial compression tests; and Section 4.4 shows a 3D slender square column subjected to external loadings at its free end.

4.1. A hexagonal cantilever beam via lattice bond model (plane stress)

To verify the reliability of the proposed calibration method in lattice bond modelling of solid materials, an example of a 2D cantilever beam subjected to complex load conditions (a transverse load F, a tensile load P, and a bending moment M) at the free end of the beam is simulated via lattice bond models.

The material and geometrical materials are as follows: (1) Youngs modulus: 21 GPa (2) shear modulus: 8.47 GPa, (3) length: 1 m, (4) height: 0.2 m. A total of 657 lattice nodes are adopted. The lattice bond stiffness values are calibrated by considering three different combinations of three uniform strain fields:

(1) SF1, a horizontal strain $\delta\varepsilon_{11}$ and a shear strain $\delta\gamma_{12}$;

(2) SF2, a vertical strain $\delta\varepsilon_{22}$ and a shear strain $\delta\gamma_{12}$;

(3) SF3, a horizontal strain $\delta\varepsilon_{11}$, a vertical strain $\delta\varepsilon_{22}$ and a shear strain $\delta\gamma_{12}$.

For all the three combined strain fields, the stiffness parameters can be computed via Eq. (19) readily but the obtained parameters are different from each other. The obtained particle-scale parameters are shown in Table 1. Note that the volume of the specimen used for calculating the strain energy in the corresponding continuum should be carefully considered, and the selection of the volume is associated with the width of the bond between particles, especially at the boundary of the specimens.

The closed-form solutions for the axial extension Δx and transverse deflection Δy of a cantilever beam based on EulerBernoulli beam theory are given by

$$\Delta x = \frac{PL}{EA}, \quad \Delta y = \frac{FL^3}{3EI} + \frac{ML^2}{2EI} \tag{27}$$

where L and A are the length and cross-section area of the cantilever beam, respectively; and E is Young's modulus. The moment of inertia I of a beam is calculated as

$$I = \begin{cases} \dfrac{ab^3}{12} & \text{(3D)} \\ \dfrac{b^3}{12} & \text{(2D)} \end{cases} \tag{28}$$

where a and b are the width and height of the beam, respectively. In this problem, a total of 4four different load combinations are considered:

Case 1: only a tensile load P=5000 kN;

Case 2: only a bending moment M =-1400 kNm;

Case 3: only a transverse load F=-5000 kN;

Case 4: both a bending moment M=-1400 kNm and a transverse load F=5000 kN.

In each load case, the bonded particle system using the parameters calibrated from one of the combined strain fields is solved until a quasi-static equilibrium state is reached. Note that the analytical solutions in Eq. (27) may no longer be valid when a large tensile load is imposed on a deflected beam, as the model may become geometrically nonlinear. Thus the tensile load condition is only simulated as a separate case in Case 3.

For comparison purposes, the formulae proposed by Griffiths and Mustoe [12] and Tavarez and Plesha [13] for estimating the particle-scale stiffnesses in a lattice structure are also used. The equations are listed below for convenience:

$$\begin{cases} k_n = \frac{Et}{\sqrt{3}(1-\nu)} \\ k_s = \frac{(1-3\nu)Et}{\sqrt{3}(1-\nu^2)} \end{cases} \text{(plane stress)} \quad \text{or} \quad \begin{cases} k_n = \frac{Et}{\sqrt{3}(1-2\nu)(1+\nu)} \\ k_s = \frac{(1-\nu)(1-4\nu)Et}{\sqrt{3}(1-2\nu)} \end{cases} \text{(plane strain)} \tag{29}$$

where t is the thickness (out of plane direction) of the model and is taken to be a unit thickness for a 2D model.

The simulated results are illustrated in Fig 5. A detailed comparison between the lattice bond simulations and the analytical solutions (from beam theory) is given in Table 1. Note that the focus of Case 1 is the axial extension

Δx, while Cases 2, 3 and 4 mainly concern the transverse deflection Δy at the right end of the cantilever beam.

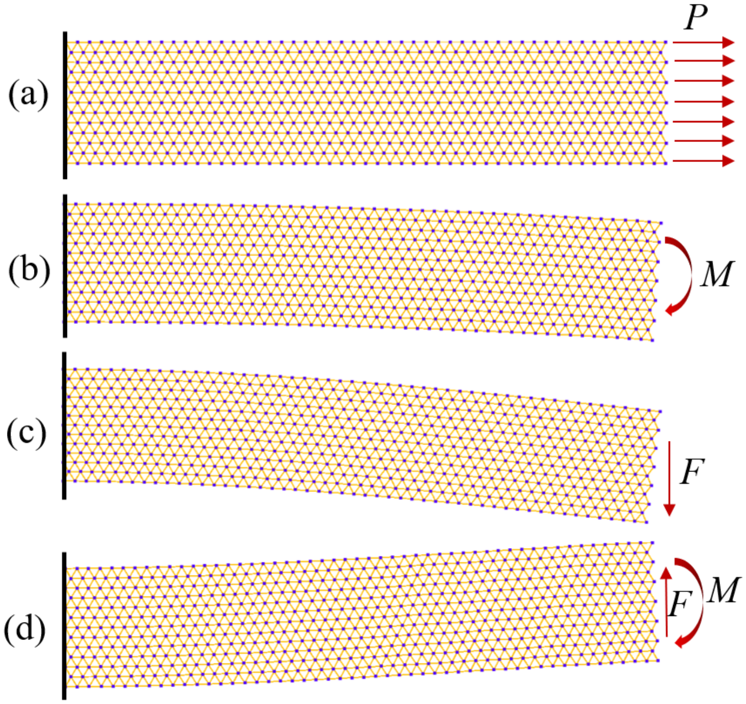

Figure 5: Hexagonal cantilever beam (a) Case 1: tensile loads; (b) Case 2: a bending moment; (c) Case 3: a transverse load and (d) Case 4: a bending moment and a transverse load

The results show that the average error of the closed-form solutions is about 6.08%, which is higher than those of the other three strain energy-based solutions. An interesting finding here is that the parameters determined by SF2 predict Case 1 with relatively large errors, and a similar situation happens when using the parameters given by SF1 for prediction in Case 2. In all three strain fields, the parameters given by SF3 yield the best predictions (an average error of 1.58%). The results indicate that the parameters should be calibrated with the strain fields as closer as possible to what are expected to occur in the system concerned. In the condition that the strain fields of the system cannot be predetermined, several basic strain fields should be accounted for in the calibration. Thus, the SF3 strain fields will be employed in the following numerical examples.

Table 1: Simulated results of cantilever beam modelling

Determination of k_n, k_s	Calibrated k_n, k_s (Pa)	Loading cases	Numerical solutions (m)	Beam theory solutions (m)	Relative Errors (%)
Closed-form solutions	1.59×10^{10}	Case 1	1.10×10^{-3}	1.05×10^{-3}	5.07
		Case 2	-0.0363	-0.0341	6.58
	3.61×10^{9}	Case 3	-0.086	-0.0811	6.08
		Case 4	0.0501	0.047	6.59
SF1 ($\delta\varepsilon_{11}$+$\delta\varepsilon_{12}$)	1.54×10^{10}	Case 1	1.06×10^{-3}	1.05×10^{-3}	0.68
		Case 2	-0.0355	-0.0341	4.11
	5.94×10^{9}	Case 3	-0.0837	-0.0811	3.23
		Case 4	0.0486	0.047	3.4
SF2 ($\delta\varepsilon_{22}$+$\delta\varepsilon_{12}$)	1.75×10^{10}	Case 1	9.92×10^{-4}	1.05×10^{-3}	7.74
		Case 2	-0.0331	-0.0341	2.85
	3.95×10^{9}	Case 3	-0.0785	-0.0811	3.2
		Case 4	0.0457	0.047	2.79
SF3 ($\delta\varepsilon_{11}$+$\delta\varepsilon_{22}$+$\delta\varepsilon_{12}$)	1.68×10^{10}	Case 1	1.0510-3	1.05×10^{-3}	0.13
		Case 2	-0.0348	-0.0341	2.12
	3.42×10^{9}	Case 3	-0.0825	-0.0811	1.77
		Case 4	0.0481	0.047	2.28

4.2. 2D uniaxial tensile test

The calibration framework is further validated with a direct tensile test of sea ice via DEM. The width and height of the specimen are 0.07 m and 0.175 m, respectively. The specimen consists of 798 circular particles with the particle radii uniformly distributed in the range from 1.68×10^{-3} m to 2.52×10^{-3} m. Each particle is cemented with its contacting particles via the parallel bond model.

The macroscopic Young's modulus and Poisson's ratio are 10 GPa and 0.3, respectively. Through the proposed calibration method based on the SF3 strain fields, the particle scale normal and tangential stiffnesses are calibrated as: 8.92×10^{9} N/m and 1.68×10^{9} N/m, respectively. Then the calibrated stiffnesses are converted to parallel bond stiffness parameters via Eq. (26).

Note that the bond strength is set to a relatively large value to ensure that the whole loading process takes place in an elastic state. The same setting is applied to all the simulations throughout this study.

When performing the test, the particles at the top and bottom rows are identified as boundary particles. The tensile loading is implemented by moving the top row particles upwards and the bottom particles downwards at a rate of 1×10^{-4} m/s. No force or displacement conditions are imposed on the lateral boundaries of the specimen. The model configuration is shown in Fig. 6.

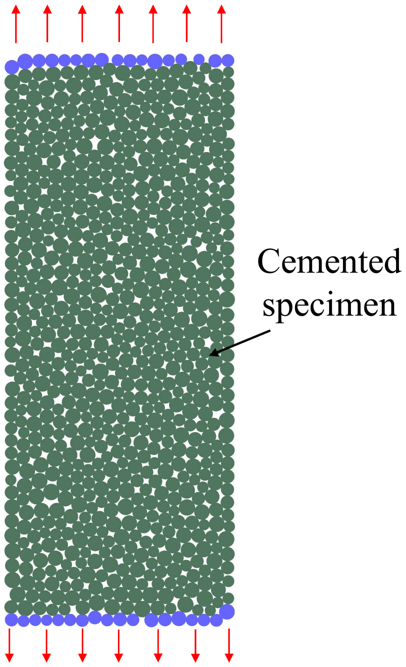

Figure 6: 2D uniaxial tension test

During testing, the stress is computed by averaging the contact forces within a measurement circle with a radius of 0.0324 m in the centre of the specimen. The strain is measured by the average relative displacements of the top and bottom boundary particles divided by the initial distance between them. The loading is terminated when an axial strain of 5×10^{-4} is reached. The stress-strain curve is shown in Fig. 7. A linear relation is observed and the corresponding Young's modulus is 1.02×10^{10} Pa, with a relative error of 2.11% compared to the targeted Youngs modulus.

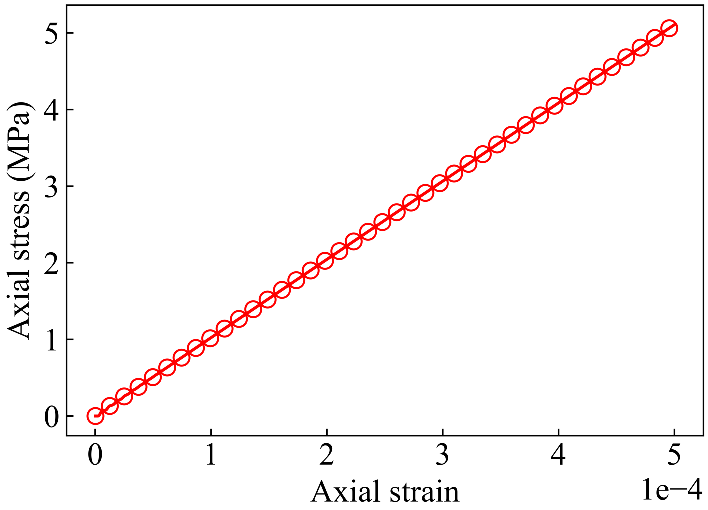

Figure 7: Stress-strain curve for the 2D uniaxial tension test

4.3. 3D uniaxial compression tests

A 3D uniaxial compression test (UCT) is performed with a parallel bond model in DEM to show the applicability of the proposed calibration framework in a 3D scenario. To generate a densely packed and well-connected assembly to reproduce a solid with highly interlocked grains, the modelling is performed with six steps:

(1) Generate initial assembly: a total of 4196 spherical particles with their radii uniformly distributed from 0.1 to 0.2 m are generated within a cubic domain.

(2) Install prescribed confining pressures: by running DEM models and moving the boundaries iteratively to develop an isotropic confining pressure of 100 kPa.

(3) Eliminating the number of floating particles: Loop through all the particles and recognise the floating particles which have a contact number less than 3. The radii of floater particles are multiplied by a factor of 1.02 and the model is rerun to an equilibrium state. Repeat the procedure until the number of floating particles is reduced to zero.

(4) Parameter calibration: Obtain the corresponding contact or bond stiffnesses based on the proposed calibration method in Section 2.

(5) Install parallel bond contacts: The parallel bond model is installed all over the assembly and the calculated parameters in Step 4 are assigned to the parallel bond model following the parameter conversion in Eq. (26). Note that inter-particle contacts are inactivated and only the parallel bond contact is adopted.

(6) Remove specimen boundary: The boundary constraints are removed, and the model is solved to an equilibrium state. Now the model generation stage terminates, and the specimen is ready for tests.

In this example, an isotropic cubic solid is simulated. The macroscopic properties are Young's modulus: 2.1×10^{10} Pa and Poisson's ratio: 0.24. By considering the SF3 combination of strain fields, the calibrated particle-scale normal and tangential stiffnesses via Eq. (19) are 1.53×10^{10} Pa, and 4.54×10^{9} Pa, respectively.

A layer of particles at each of the six boundaries of the specimen is recognised as a boundary plate. The loadings are implemented by moving the boundary particles at a fixed rate. For example, as shown in Fig. 8, the upper plate moves downwards, and the bottom plate moves upwards to impose the compressive force along the vertical direction. Note that three separate groups of loadings along different directions (x, y, and z directions in the global coordinate frame) are required to obtain Young's modulus in each direction. The strain is computed by dividing the initial distance between the two loading plates by the relative average displacements between them. The stress is measured by creating a measurement sphere in the centre of the specimen and by averaging the contact forces within the sphere.

The stress-strain curves along the three directions are shown in Fig. 9. It is found that the specimen exhibits a linear elastic behaviour as there is no irreversible damage happening at such a small strain range. The slope of each stress-strain curve represents Youngs modulus in this direction. The obtained three Youngs moduli can be found in Table 2. An average error of 3.92% in the three directions demonstrates that the bond-scale parameters are well-calibrated by the proposed method.

Note that the UCTs in this section are simulated only with particles and no wall elements are involved. If the contact parameters between particles and wall elements need to be considered in the calibration procedure, the verification problem should incorporate the particle-wall contacts, and vice versa.

Table 2: Simulated results of UCTs

Direction	Targeted Youngs modulus (Pa)	Actual Youngs modulus (Pa)	Relative error (%)
x	2.1×10^{10}	20364364798	3.03
y		20522670058	2.2
z		19646465027	6.4

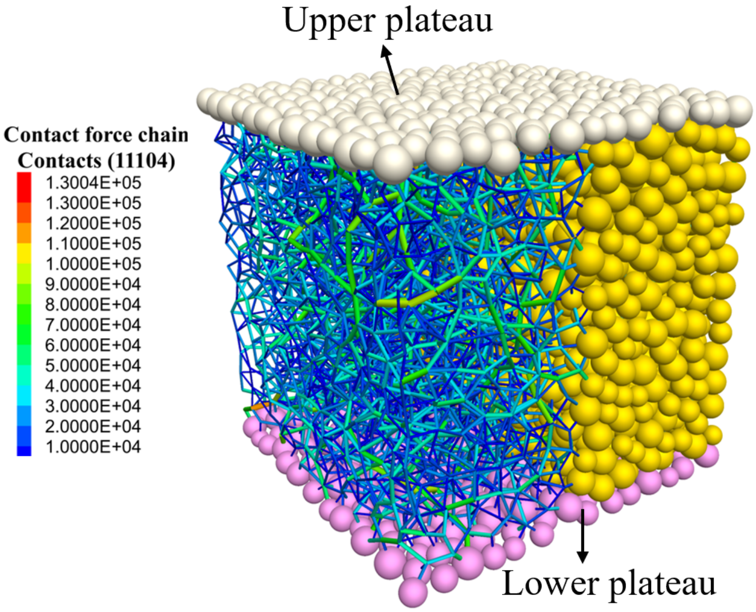

Figure 8: Uniaxial compression tests

4.4. 3D slender square column

A 3D slender square beam simulated with bonded DEM is employed as the final example to validate the calibration method. The height and width (side length of a square) of the column are 1.44 m and 0.2 m, respectively. The base end of the column is fixed while the top end can move freely.

A total of 7300 spherical particles are used to simulate the column, with the radius and the density of particles being 1 cm and 2600 kg/m3. The macroscopic Young's modulus and Poisson's ratio are 22.1 GPa and 0.24, respectively. By using the proposed calibration method, the bond-scale normal and tangential stiffnesses are found to be 4.513×10^{10} N/m and 3.592×10^{10} N/m, respectively. The corresponding parallel bond stiffnesses for each bond

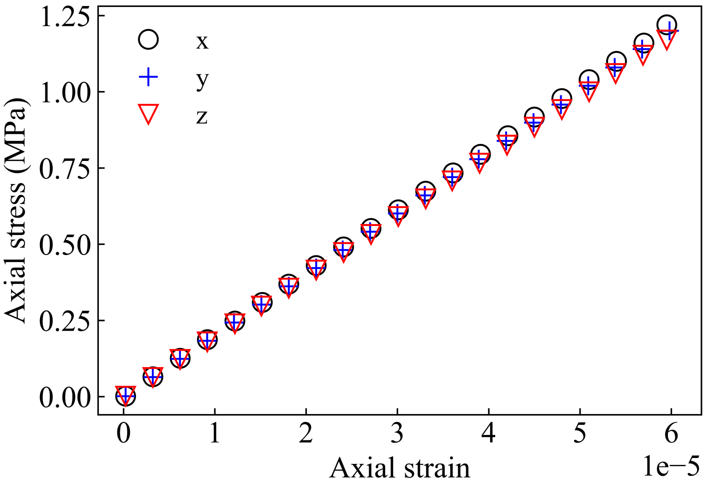

Figure 9: Small-strain stress-strain relation for a cubic solid

are calculated via Eq. (26) and assigned accordingly.

We consider three different loading conditions at the top of the specimen: Case 1: a horizontal load; Case 2: uniform pull loads; and Case 3: a bending moment. These loads are uniformly imposed on the top end of the specimen. The simulated results are provided in Table 3, after the specimen reaches a static equilibrium state. The cross-section and final deformation state of the column are depicted in Fig. 10. The simulated results are compared with the analytical solutions given by Eqs. (27)-(28) and an average error of about 6.08% is found for the three loading cases. Note that Cases 1 and 3 focus on the transverse deflection Δy while Case 2 mainly concerns the axial extension Δz at the free end of the column. These results further confirm the reliability of the proposed calibration framework.

Table 3: Simulated results of 3D slender square column modelling

Case	Loads	Numerical solutions (m)	Analytical solutions (m)	Relative error (%)
Case 1	$F_y = -3 \times 10^9$ N	-0.101	-0.107	5.61
Case 2	$P = 1 \times 10^{11}$ N	0.016	0.017	5.88
Case 3	$M_x = -2 \times 10^{11}$ Nm	0.069	0.074	6.76

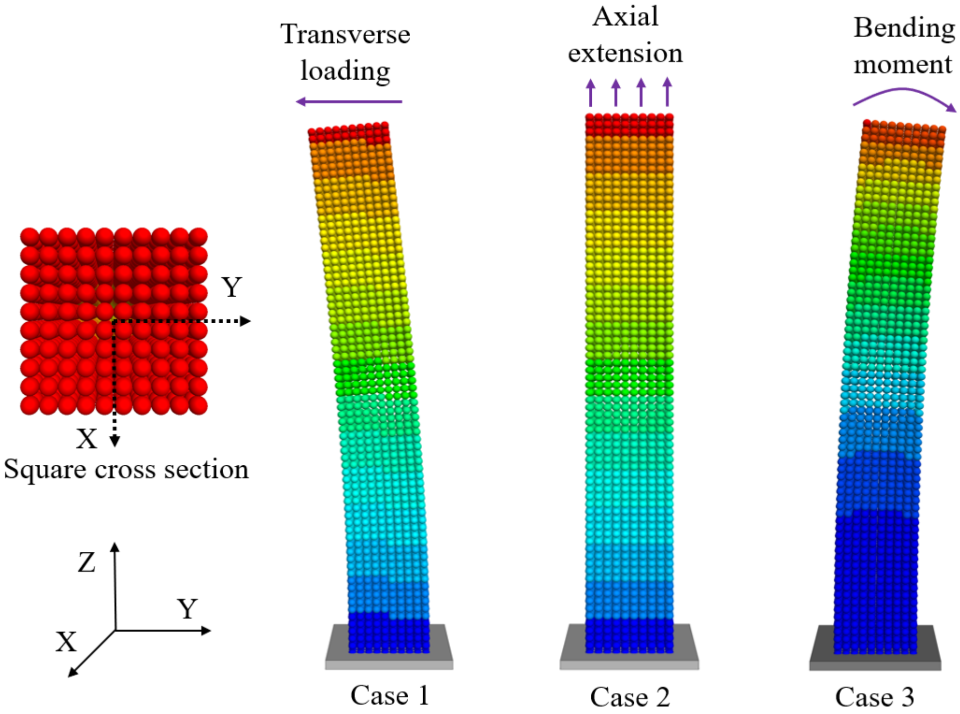

Figure 10: The cross section and final deformation state of the simulated slender columns

5. Discussion

In the preceding section, four different simulations have been employed to verify the reliability of the proposed calibration framework. The optimal calibrated parameters can be obtained efficiently by solving a system of two linear equations in each case. Thus convergence is always guaranteed in the current framework. Also, a unique solution exists for a given packing subjected to a certain combination of external deformation fields in our proposed framework, although different selections of strain fields will yield different unique solutions. In this section, a few more aspects of the proposed calibration procedure are discussed below.

5.1. The origins of calibration error in the proposed framework

Although the calibrated parameters can reproduce the desired macroscopic elastic property satisfactorily, there is always a small discrepancy between the discrete and continuum systems. A few reasons might be responsible for this error.

Firstly, a global strain occurring throughout a continuum is assumed to be the same as the local strain of all interactions in the corresponding discrete system. However, in lattice/particle bonded models, external loads are transferred in an inhomogeneous force-chain way. The actual strain field occurring in the models can be highly complicated. Secondly, the selection of strain fields relates to calibration accuracy. When the parameters are calibrated with the strain fields that the discrete system will exactly experience, relatively high accuracy can be expected. As it is not straightforward to precisely characterise the strain fields in a boundary value problem (BVP), we often can only make use of several basic strain fields for calibration. In this study, all the verification examples adopt uniform fields by considering their combinations of several compression or shear strain fields.

Note that only normal and tangential relative displacements between particles are considered in this work. The interparticle rotation or twisting can also store deformation energy if rotation-related bond interactions are considered. The additional parameters involved can also be calibrated within the proposed framework.

5.2. The alternative linear elastic parameters represented with Young's modulus and stiffness ratio

In addition to normal and tangential stiffnesses, an alternative way to characterise particle-scale elastic parameters in bonded DEM is by using particle-scale Young's modulus E^* and the normal to tangential stiffness ratio k^*. These two sets of representation methods are interchangeable. For a bond k, we have:

$$k_n = AE^*/L^{(k)} \tag{30}$$

$$k_{\mathrm{s}} = k_n/k^* \tag{31}$$

$$A = \left\{ \begin{array}{ll} \pi\bar{R}^2 & (\text{3D}) \\ 2\bar{R} & (\text{2D}) \end{array} \right. , \bar{R} = \min\left(R^{(1)}, R^{(2)}\right) \tag{32}$$

By substituting Eqs. (30-31) into Eq. (15), the original loss function can be formulated as:

$$\mathbb{L} = \frac{1}{4}\Bigg\{ \int_{\Omega} C_{ijkl}\varepsilon_{kl}\varepsilon_{ij}d\Omega - \sum_{k=1}^{N_c} AE^* L^{(k)} \Bigg[\left(\varepsilon_{ij}\xi_i^{(k)}\xi_j^{(k)}\right)\left(\varepsilon_{kl}\xi_k^{(k)}\xi_l^{(k)}\right) + \left(\varepsilon_{mn}\xi_n^{(k)} - \varepsilon_{ij}\xi_i^{(k)}\xi_j^{(k)}\xi_m^{(k)}\right)\left(\varepsilon_{mk}\xi_k^{(k)} - \varepsilon_{lk}\xi_l^{(k)}\xi_k^{(k)}\xi_m^{(k)}\right)/k^* \Bigg] \Bigg\}^2 \tag{33}$$

The gradients of L to E^* and k^* can be analytically derived from Eq. (33). The optimal particle-scale parameters can be found by enforcing the first-order gradients to be zero under two imposed independent strain fields.

5.3. Extending to nonlinear elastic (Hertz-type) calibration

The bond behaviour can be linear or non-linear. The magnitude of the normal force f_n of a non-linear elastic model is formulated as:

$$f_n = \frac{2(2\bar{R})^{1/2} G^*}{3\,(1 - v^*)} \left(\Delta u_n\right)^{\alpha_h} \tag{34}$$

where α_h is a power-law exponent with $\alpha_h > 1$. The selection of α_h depends on different scenarios. For the Hertz-type model, $\alpha_h = 1.5$.

For the tangential direction, the magnitude of the tangential force f_s is proportional to the tangential displacement within the Coulomb limit:

$$\Delta f_s = k_s \Delta u_s \tag{35}$$

The analytical expression of a tangential stiffness is difficult to precisely determine because it is associated with normal interaction forces and preceding sliding history. There are currently a few different formulations for tangential stiffnesses in the literature [51, 52, 53, 54]. Here, a widely used equation for the nonlinear elastic tangential stiffness k_s is adopted [53]:

$$k_s = \frac{2\,(1 - \nu^*)}{2 - \nu^*} \alpha_h \left[\frac{2G^* \sqrt{2\bar{R}}}{3\,(1 - \nu^*)} \right]^{1/\alpha_h} \left(f_n\right)^{(\alpha_h - 1)/\alpha_h} \tag{36}$$

Then the strain energy stored in a nonlinear elastic model can be expressed as:

$$U = \frac{\alpha_\mathrm{h}}{(\alpha_\mathrm{h} + 1)} \frac{\left(f_n\right)^2}{k_n} + \frac{1}{2} \frac{\left(f_s\right)^2}{k_s} \tag{37}$$

In the case of the Hertz-type model, the normal and tangential stiffnesses can be reformulated as:

$$k_n = \frac{\partial f_n}{\partial \delta_n} = \frac{(2\bar{R})^{1/2} G^*}{(1 - \nu^*)} \delta_n^{1/2} = \left[\frac{3\bar{R} G^{*2}}{(1 - \nu^*)^2} \right]^{1/3} \left(f_n\right)^{1/3} \tag{38}$$

$$k_s = 2(G^*)^{(2/3)} \left[3\,(1 - \nu^*)\,\bar{R} f_n \right]^{1/3} / \left(2 - \nu^*\right) \tag{39}$$

The strain energy inside the whole specimen is given by:

$$U_{\mathrm{d}} = \sum_{k=1}^{N_c} \left\{ \frac{3}{5} \left[\frac{\left(1-\nu^*\right)^2}{3\bar{R}G^{*2}} \right]^{1/3} \left(\Delta u_n^{(k)}\right)^{5/3} + \frac{G^{*(2/3)} \left[3\left(1-\nu^*\right)\bar{R}f_n^{(k)}\right]^{1/3}}{\left(2-\nu^*\right)} \left(\Delta u_{\mathrm{s}}^{(k)}\right)^2 \right\} \tag{40}$$

The loss function then becomes:

$$\mathbb{L} = \left\langle \frac{1}{2}\int_\Omega C_{ijkl}\varepsilon_{kl}\varepsilon_{ij}d\Omega - \sum_{k=1}^{N_c} \left\{ \frac{3}{5} \left[\frac{\left(1-\nu^*\right)^2}{3\bar{R}G^{*2}} \right]^{1/3} \left(\Delta u_n^{(k)}\right)^{5/3} + \frac{G^{*(2/3)} \left[3\left(1-\nu^*\right)\bar{R}f_n^{(k)}\right]^{1/3}}{\left(2-\nu^*\right)} \left(\Delta u_{\mathrm{s}}^{(k)}\right)^2 \right\} \right\rangle^2 \tag{41}$$

By considering the relation between the strain tensor and the interparticle displacements in Eqs. (6) and (8), the strain energy within a solid specimen (Eq. (40)) can be represented with the macroscopic strain directly. Then the gradients of the loss function $\mathbb{L}$ to G^* and ν^* can be analytically obtained by using symbolic computation, via, e.g., Mathematica or SymPy package in Python. However, the derived gradients are also nonlinear and an iterative procedure, such as Newton-Raphson, may need to be used to find the optimal solutions.

5.4. Extending to the calibration of particle-wall contact parameters

Although all the analytical derivations and numerical examples above only involve particle-particle contacts, the proposed framework can be applied to the calibration of particle-wall contacts as well. Then the strain energy stored in particle-wall contacts should be counted as part of the strain energy in the discrete system. Also, each contact length $L^{(k)}$ should be the distance between the particle and the wall. In the case that the particle-particle contact parameters equal to those of particle-wall contacts or both types of parameters have a quantitative relation between them, two mutually independent strain fields are sufficient to calibrate the parameters. In the case that particle-wall contact parameters do not equal to those of particle-particle contacts and no explicit relation is predefined between them, at least four mutually different strain fields are required.

6. Concluding remarks

In this study, a generic strain energy-based calibration framework with novelties in several aspects has been proposed to calibrate the elastic parameters of particle-based modelling for solid materials. The approach is developed based on the idea of minimising the difference of strain energy between the discrete and continuum systems under certain strain deformations. Different from all the existing calibration methods, the proposed method offers an innovative solution for the parameter calibration of discrete element modelling or lattice bond modelling by taking full account of the actual microstructure of the model. The flexibility of strain fields selected for calibration also provides a chance to enable the calibrated parameters to suit all kinds of potential deformation conditions. Particularly, the calibration efficiency of this approach resembles the need of solving only a linear system of equations but has better applicability than traditional analytical methods. The calibration accuracy is close to advanced surrogate models or optimisation-based methods with many tentative simulations, but the proposed framework is much more efficient.

The idea of decoupling is one of important reasons contributing to high calibration efficiency of the proposed method. As we have stated in Section 2.1, all the parameters to be calibrated are decoupled as elastic and strength parameters. The focus of this study is the calibration of elastic parameters, while the other irreversible deformation phenomenon, such as evolving particle positions and brittle damage (e.g. bond breakage) are related to strength parameters and thus not considered. For the calibration of strength parameters, one may refer to the physics-informed optimisation framework reported in our previous work [45].

The proposed method can be easily implemented. Without resorting to the aid of third-party packages or software, the proposed method only requires simple computations associated with the microstructural information of a given particle/lattice system. Thus, the method can be readily implemented not only in in-house codes but also in all major DEM computation packages.

As having been described and verified, the proposed method is well applicable to circular/spherical particle-based packings, irrespective of loose or dense, monodisperse or polydisperse specimens. However, in this study the elastic strain energy in a discrete system is analytically calculated for discs/spheres based on a uniform strain homogenization assumption, to ensure an efficient calibration without involving extra computational costs. For non-spherical particles, it may not be easy to determine the elastic strain energy in an analytical way. Instead, one may consider quantifying the strain energy in a numerical manner. In addition to non-spherical particles and the possible extensions discussed in Section 5, the calibration of anisotropic elasticity and non-uniform normal and tangential interaction stiffnesses can also be considered within the proposed framework. All these possibilities will be further exploited and examined in our future work.

Acknowledgement

The study was financially supported by National Natural Science Foundation of China (via General Project #11972030) and Research Grants Council of Hong Kong (under GRF #16208720). Part of this work was financially supported by the Project of Hetao Shenzhen-Hong Kong Science and Technology Innovation Cooperation Zone (HZQB-KCZYB-2020083).

References

[1] T. Kawai, New element models in discrete structural analysis, Journal of the Society of Naval Architects of Japan 1977 (141) (1977) 174–180.

[2] G. A. D'Addetta, F. Kun, E. Ramm, On the application of a discrete model to the fracture process of cohesive granular materials, Granular matter 4 (2) (2002) 77–90.

[3] M. Wang, A scale-invariant bonded particle model for simulating large deformation and failure of continua, Computers and Geotechnics 126 (2020) 103735.

[4] M. Nitka, J. Tejchman, Modelling of concrete behaviour in uniaxial compression and tension with dem, Granular Matter 17 (1) (2015) 145–164.

[5] E. Oate, F. Zrate, J. Miquel, M. Santasusana, M. A. Celigueta, F. Arrufat, R. Gandikota, K. Valiullin, L. Ring, A local constitutive model for the discrete element method. application to geomaterials and concrete, Computational particle mechanics 2 (2) (2015) 139–160.

[6] B. Chen, J. Xiang, J.-P. Latham, R. R. Bakker, Grain-scale failure mechanism of porous sandstone: an experimental and numerical fdem study of the brazilian tensile strength test using ct-scan microstructure, International Journal of Rock Mechanics and Mining Sciences 132 (2020) 104348.

[7] T. Kazerani, J. Zhao, A microstructure-based model to characterize micromechanical parameters controlling compressive and tensile failure in crystallized rock, Rock mechanics and rock engineering 47 (2) (2014) 435–452.

[8] B. Chen, J. Xiang, J.-P. Latham, Influence of inter-grain cementation stiffness on the effective elastic properties of porous bentheim sandstone, Journal of Rock Mechanics and Geotechnical Engineering (2022). doi:https://doi.org/10.1016/j.jrmge.2022.06.009.

[9] Y. Tan, D. Yang, Y. Sheng, Discrete element method (dem) modeling of fracture and damage in the machining process of polycrystalline sic, Journal of the European ceramic society 29 (6) (2009) 1029–1037.

[10] S. Ji, S. Di, X. Long, Dem simulation of uniaxial compressive and flexural strength of sea ice: Parametric study, Journal of Engineering Mechanics 143 (1) (2017) C4016010.

[11] C. Coetzee, Calibration of the discrete element method, Powder Technology 310 (2017) 104–142.

[12] D. Griffiths, G. G. Mustoe, Modelling of elastic continua using a grillage of structural elements based on discrete element concepts, International Journal for Numerical Methods in Engineering 50 (7) (2001) 1759–1775.

[13] F. A. Tavarez, M. E. Plesha, Discrete element method for modelling solid and particulate materials, International journal for numerical methods in engineering 70 (4) (2007) 379–404.

[14] B. D. Le, G. Koval, C. Chazallon, Discrete element model for crack propagation in brittle materials, International Journal for Numerical and Analytical Methods in Geomechanics 40 (4) (2016) 583–595.

[15] G. Zhao, J. Fang, J. Zhao, A 3d distinct lattice spring model for elasticity and dynamic failure, International Journal for Numerical and Analytical Methods in Geomechanics 35 (8) (2011) 859–885.

[16] K. Jarolin, M. Dosta, Linearization-based methods for the calibration of bonded-particle models, Computational particle mechanics 8 (3) (2021) 511–523.

[17] Z. Han, D. Weatherley, R. Puscasu, A relationship between tensile strength and loading stress governing the onset of mode i crack propagation obtained via numerical investigations using a bonded particle model, International Journal for Numerical and Analytical Methods in Geomechanics 41 (18) (2017) 1979–1991.

[18] S. Chehreghani, M. Noaparast, B. Rezai, S. Z. Shafaei, Bonded-particle model calibration using response surface methodology, Particuology 32 (2017) 141–152.

[19] T. Kazerani, J. Zhao, Micromechanical parameters in bonded particle method for modelling of brittle material failure, International journal for numerical and analytical methods in geomechanics 34 (18) (2010) 1877–1895.

[20] Y. Wang, F. Tonon, Modeling lac du bonnet granite using a discrete element model, International Journal of Rock Mechanics and Mining Sciences 46 (7) (2009) 1124–1135. doi:10.1016/j.ijrmms.2009.05.008.

[21] Z. Xu, Z. Wang, W. Wang, P. Lin, J. Wu, An integrated parameter calibration method and sensitivity analysis of microparameters on mechanical behavior of transversely isotropic rocks, Computers and Geotechnics 142 (2022) 104573.

[22] C. Xu, X. Liu, E. Wang, S. Wang, Calibration of the microparameters of rock specimens by using various machine learning algorithms, International Journal of Geomechanics 21 (5) (2021) 04021060.

[23] A. Truszkowska, Q. Yu, P. A. Greaney, T. M. Evans, J. J. Kruzic, A discrete element method representation of an anisotropic elastic continuum, Journal of the Mechanics and Physics of Solids 121 (2018) 363–386.

[24] D. S. Nasato, R. Q. Albuquerque, H. Briesen, Predicting the behavior of granules of complex shapes using coarse-grained particles and artificial neural networks, Powder Technology 383 (2021) 328–335.

[25] A. Boikov, R. Savelev, V. Payor, Dem calibration approach: Random forest, in: Journal of Physics: Conference Series, Vol. 1118, IOP Publishing, 2018, p. 012009.

[26] F. Westbrink, A. Elbel, A. Schwung, S. X. Ding, Optimization of dem parameters using multi-objective reinforcement learning, Powder Technology 379 (2021) 602–616.

[27] H. Cheng, T. Shuku, K. Thoeni, P. Tempone, S. Luding, V. Magnanimo, An iterative bayesian filtering framework for fast and automated calibration of dem models, Computer methods in applied mechanics and engineering 350 (2019) 268–294.

[28] H. Cheng, T. Shuku, K. Thoeni, H. Yamamoto, Probabilistic calibration of discrete element simulations using the sequential quasi-monte carlo filter, Granular matter 20 (1) (2018) 1–19.

[29] P. Hartmann, H. Cheng, K. Thoeni, Performance study of iterative bayesian filtering to develop an efficient calibration framework for dem, Computers and Geotechnics 141 (2022) 104491.

[30] K. J. Hanley, C. O'Sullivan, J. C. Oliveira, K. Cronin, E. P. Byrne, Application of taguchi methods to dem calibration of bonded agglomerates, Powder technology 210 (3) (2011) 230–240.

[31] J. Yoon, Application of experimental design and optimization to pfc model calibration in uniaxial compression simulation, International Journal of Rock Mechanics and Mining Sciences 44 (6) (2007) 871–889.

[32] T. Kazerani, Effect of micromechanical parameters of microstructure on compressive and tensile failure process of rock, International Journal of Rock Mechanics and Mining Sciences 64 (2013) 44–55.

[33] R. Chen, Y. Wang, R. Peng, S. Jiang, C. Hu, Z. Zhao, Identification of the discrete element model parameters for rock-like brittle materials, Computer Modeling in Engineering & Sciences 123 (2) (2020) 717–737.

[34] M. Rackl, K. J. Hanley, A methodical calibration procedure for discrete element models, Powder technology 307 (2017) 73–83.

[35] M. Wang, P. Cao, Calibrating the micromechanical parameters of the pfc2d (3d) models using the improved simulated annealing algorithm, Mathematical Problems in Engineering 2017 (2017).

[36] H. Fathipour-Azar, Machine learning-assisted distinct element model calibration: Anfis, svm, gpr, and mars approaches, Acta Geotechnica 17 (4) (2022) 1207–1217.

[37] R. Chen, J. Li, Y. Qian, R. Peng, S. Jiang, C. Hu, Z. Zhao, An effective inverse procedure for identifying demparameters of rock-like materials, Mathematical Problems in Engineering 2019 (2019).

[38] C. Pan, X. Li, L. He, J. Li, Study on the effect of micro-geometric heterogeneity on mechanical properties of brittle rock using a grain-based discrete element method coupling with the cohesive zone model, International Journal of Rock Mechanics and Mining Sciences 140 (2021) 104680.

[39] M. Wang, Z. Lu, W. Wan, Y. Zhao, A calibration framework for the microparameters of the dem model using the improved pso algorithm, Advanced Powder Technology 32 (2) (2021) 358–369.

[40] H. Q. Do, A. M. Aragn, D. L. Schott, A calibration framework for discrete element model parameters using genetic algorithms, Advanced Powder Technology 29 (6) (2018) 1393–1403.

[41] M. De Simone, L. M. Souza, D. Roehl, Estimating dem microparameters for uniaxial compression simulation with genetic programming, International Journal of Rock Mechanics and Mining Sciences 118 (2019) 33–41.

[42] Y. Wang, F. Tonon, Calibration of a discrete element model for intact rock up to its peak strength, International journal for numerical and analytical methods in geomechanics 34 (5) (2010) 447–469.

[43] C. Richter, T. Roessler, G. Kunze, A. Katterfeld, F. Will, Development of a standard calibration procedure for the dem parameters of cohesionless bulk materialspart ii: Efficient optimization-based calibration, Powder Technology 360 (2020) 967–976.

[44] T. Qu, Y. Feng, T. Zhao, M. Wang, A hybrid calibration approach to hertz-type contact parameters for discrete element models, International Journal for Numerical and Analytical Methods in Geomechanics 44 (9) (2020) 1281–1300.

[45] T. Qu, Y. Feng, M. Wang, S. Jiang, Calibration of parallel bond parameters in bonded particle models via physics-informed adaptive moment optimisation, Powder Technology 366 (2020) 527–536. doi:10.1016/j.powtec.2020.02.077.

[46] D. O. Potyondy, P. A. Cundall, A bonded-particle model for rock, International Journal of Rock Mechanics and Mining Sciences 41 (8) (2004) 1329–1364. doi:10.1016/j.ijrmms.2004.09.011.

[47] M. Xia, C.-b. Zhao, Simulation of rock deformation and mechanical characteristics using clump parallel-bond models, Journal of Central South University 21 (7) (2014) 2885–2893.

[48] Y. Peng, H. Liu, C. Li, X. Ding, X. Deng, C. Wang, The detailed particle breakage around the pile in coral sand, Acta Geotechnica 16 (6) (2021) 1971–1981.

[49] Y. Peng, X. Ding, Z.-Y. Yin, P. Wang, Micromechanical analysis of the particle corner breakage effect on pile penetration resistance and formation of breakage zones in coral sand, Ocean Engineering 259 (2022) 111859. doi:https://doi.org/10.1016/j.oceaneng.2022.111859.

[50] Itasca, Pfc3d (particle flow code in 3 dimensions), version 5.0, Minneapolis: ICG (2014).

[51] S. Yimsiri, K. Soga, Micromechanics-based stress strain behaviour of soils at small strains, Geotechnique 50 (5) (2000) 559–671.

[52] C. S. Chang, S. S. Sundaram, A. Misra, Initial moduli of particulated mass with frictional contacts, International Journal for Numerical and Analytical Methods in Geomechanics 13 (6) (1989) 629–644.

[53] P. Cundall, Computer simulations of dense sphere assemblies, Vol. 20, Elsevier, 1988, pp. 113–123.

[54] Y. Tsuji, T. Tanaka, T. Ishida, Lagrangian numerical simulation of plug flow of cohesionless particles in a horizontal pipe, Powder technology 71 (3) (1992) 239–250.